Quantitative live-cell imaging and 3D modeling reveal critical functional features in the cytosolic complex of phagocyte NADPH oxidase

Cornelia S. Ziegler[1], Leila Bouchab[1], Marc Tramier[2], Dominique Durand[3], Franck Fieschi[4] Sophie Dupré-Crochet[1], Fabienne Mérola[1], Oliver Nüße[1,*], Marie Erard[1,*]

From the [1]Laboratoire de Chimie Physique, CNRS, Univ. Paris-Sud, Université Paris-Saclay, 91405, Orsay France, [2]Univ Rennes, CNRS, IGDR [(Institut de génétique et développement de Rennes)] – UMR 6290, BIOSIT – UMS 3480, F-35000 RENNES, France, [3]Institute for Integrative Biology of the Cell (I2BC), CEA, CNRS UMR 9198, Univ. Paris-Sud, Université Paris-Saclay, Gif-sur-Yvette, France, [4]Univ. Grenoble Alpes, CNRS, CEA, Institut de Biologie Structurale, F-38044 Grenoble, France

Running title: *a new 3D model of the NADPH oxidase cytosolic complex*

[*]to whom correspondence should be addressed: Marie Erard; marie.erard@u-psud.fr or Oliver Nüsse; oliver.nusse@u-psud.fr

Keywords : intrinsically disordered proteins ; unstructured domain; quaternary structure; NOX family; NADPH oxidase; protein-protein interaction; FRET-FLIM; FCCS; fluorescent protein

ABSTRACT

Phagocyte NADPH oxidase produces superoxide anions, a precursor of reactive oxygen species (ROS) critical for host responses to microbial infections. However, uncontrolled ROS production contributes to inflammation, making NADPH oxidase a major drug target. It consists of two membranous (Nox2 and $p22^{phox}$) and three cytosolic subunits ($p40^{phox}$, $p47^{phox}$, and $p67^{phox}$) that undergo structural changes during enzyme activation. Unraveling the interactions between these subunits and the resulting conformation of the complex could shed light on NADPH oxidase regulation and help identify inhibition sites. However, the structures and the interactions of flexible proteins comprising several well-structured domains connected by intrinsically disordered protein segments are difficult to investigate by conventional techniques such as X-ray crystallography, NMR, or cryo-EM. Here, we developed an analytical strategy based on FRET–fluorescence lifetime imaging (FLIM) and fluorescence cross-correlation spectroscopy (FCCS) to structurally and quantitatively characterize NADPH oxidase in live cells. We characterized the inter- and intramolecular interactions of its cytosolic subunits by elucidating their conformation, stoichiometry, interacting fraction, and affinities in live cells. Our results revealed that the three subunits have a 1:1:1 stoichiometry and that nearly 100% of them are present in complexes in living cells. Furthermore, combining FRET data with small-angle X-ray scattering (SAXS) models and published crystal structures of isolated domains and subunits, we built a 3D model of the entire cytosolic complex. The model disclosed an elongated complex containing a flexible hinge separating two domains ideally positioned at one end of the complex and critical for oxidase activation and interactions with membrane components.

Numerous proteins contain intrinsically disordered regions (1,2). Their growing number challenges the paradigm of a strong relationship between structure and function. Those proteins require new strategies to study their shape and their interactions. Here we focus on proteins composed of structured domains linked by disordered segments. Those segments and thus the whole protein can adopt a broad ensemble of conformations. These ensembles are highly influenced by their environment. In particular, the molecular crowding, the local ion concentrations, pH or viscosity present in live cells may change the set of accessible conformations. Nevertheless, when they are associated with diseases, knowledge about both their structure and their affinity with partners is essential to identify potential drug targets in medicinal chemistry. Their structural analysis calls for new *in situ* analytical strategies (1,2). Here, we combined live cell FRET-FLIM and FCCS approaches to propose an integrated analytical workflow for structural and quantitative studies of a protein complex composed of such multi-domain proteins in their native environment. We applied this workflow to the intra- and inter-molecular interactions of the cytosolic factors of the phagocyte NADPH oxidase complex.

The phagocyte NADPH oxidase is one of the seven isoforms of the Nox family and a major

Accepted manuscript

enzyme of the immune system due to its pronounced production of microbicidal reactive oxygen species (ROS). A pathological hyperactivity of this oxidase leads to chronic inflammation, which is associated with cardiovascular diseases, stroke, and chronic obstructive pulmonary disease (COPD) (3). The activity is regulated by the spatio-temporal organization of the intra- and intermolecular interactions of its cytosolic subunits, $p40^{phox}$, $p47^{phox}$, and $p67^{phox}$, forming a soluble complex before activation. Upon activation, these subunits translocate together with the small GTPase Rac to the membrane subunits Nox2 and $p22^{phox}$ to form the active oxidase complex. The protein interactions within the cytosolic complex were extensively studied *in vitro* (Fig. 1) (3). In addition to the interactions between $p40^{phox}$ and $p67^{phox}$ or $p47^{phox}$ and $p67^{phox}$, an interaction between the SH3 domain of $p40^{phox}$ and the PRR domain of $p47^{phox}$ has been observed but its physiological relevance is not clear (4). The structure of $p40^{phox}$ was entirely solved (5). The presence of intrinsically disordered regions in $p47^{phox}$ and $p67^{phox}$, predicted from their sequence (6), prevented the crystallization of the whole subunits. Only domains either isolated or in interaction were solved (3). To date, neither the spatial organization nor the stoichiometric composition of the entire complex in live cells was clarified. Using live cell FRET-FLIM and FCCS approaches with fluorescent protein-tagged subunits, we demonstrated a 1:1:1 stoichiometry of the three subunits, estimated their affinity and analyzed their spatial organization. Finally, we used these findings to elaborate a new 3D *in silico* model of the entire cytosolic complex in the live cell situation. This model shows an elongated complex and a flexible hinge. It is fully compatible with the multiple steps of oxidase activation. In addition, it can guide the identification of potential sites for anti-inflammatory drug targets to regulate the NADPH oxidase activity.

Results

FP tagged subunits are correctly expressed and are functional

The cytosolic subunits $p40^{phox}$, $p47^{phox}$ and $p67^{phox}$ were tagged with fluorescent proteins (FPs, Table S*1*), either cyan (CFP: mTurquoise or Aquamarine) (7), yellow (YFP: Citrine) (8), or red (RFP: mCherry) (9). The size of the fusion proteins expressed by COS7 cells was verified by Western Blot (Fig. S1*A*). To assess whether the FP-labelled subunits are able to reconstitute the active oxidase complex, we used $COS^{Nox2/p22}$ cells stably expressing the membranous subunits $Nox2/p22^{phox}$ and Rac, but no endogenous cytosolic subunits (10). $COS^{Nox2/p22}$ were transiently transfected with the three cytosolic subunits with or without a FP-tag (Fig. 2*A*). The production of superoxide anions was monitored by a luminometry assay sensitive to extracellular ROS (Fig. 2*B*). The ROS production started upon activation with phorbol myristate acetate (PMA) and stopped immediately after addition of diphenyleneiodonium (DPI), a NADPH oxidase inhibitor. All constructs allowed a pronounced ROS production (Fig. 2*C*). The production with N-terminal tagged $p47^{phox}$ and $p67^{phox}$ was lower in comparison to the C-terminal tagged variants but still much higher than the non-transfected cells. The presence of the FP-tags slowed down the ROS production and consequently delayed the time point at which the maximal signal was reached (Fig. S1*B* and *C*). Taken together, these observations show that all our FP-tagged subunits are able to reconstitute an active NADPH oxidase complex and are fully suitable to explore their spatial organization and affinity.

Förster resonance energy transfer (FRET) is observed between fluorescent proteins at both ends of individual subunits and is not strongly modified in presence of their partners.

We then tagged each of the cytosolic subunits $p40^{phox}$, $p47^{phox}$ and $p67^{phox}$ simultaneously at both termini with a donor (D) and an acceptor (A) FP for Förster resonance energy transfer (FRET), resulting in so-called tandems (schemes Fig. 3, Table S1). We used as a positive control a simple D/A tandem in which the donor and acceptor FPs were linked by a flexible 27 amino acids long peptide (11). Tandems were expressed in COS7 cells and FRET was monitored by fluorescence lifetime imaging (FLIM). The apparent FRET efficiencies, E_{app}, were derived from the average fluorescence lifetime of the donor FP measured in individual cells (Eq. 1 to 3 in experimental procedures). E_{app} for the $p40^{phox}$, $p47^{phox}$ and $p67^{phox}$ tandems were significant, although lower than in the simple D/A tandem (E_{app} = 8.2 ± 1.2%, 12.3 ± 1.2%, 7.7 ± 1.1 % and 32.7 ± 1.8%, respectively, Fig. 3*B*). The low E_{app} values for the subunit tandems are consistent with the much larger size of the central subunits as compared to a 27 amino acids peptide linker.

Next, we studied the influence of the $p67^{phox}$ partner on the $p47^{phox}$ tandem and of $p40^{phox}$ on the $p67^{phox}$ tandem. Either $p47^{phox}$ or $p67^{phox}$ tandems were co-expressed with a plasmid coding for the partner subunit connected to RFP *via* the viral P2A peptide (12,13). The P2A sequence prevents the peptide bond formation and leads to the separate expression of the subunit and the RFP, the presence of the RFP proving the correct expression of the partner subunit. The

Accepted manuscript

co-expression of tandems with RFP alone was taken as reference (Fig. 3*C*). The co-expression of RFP-2A-p67^{phox} did not change the apparent FRET efficiency in the p47^{phox} tandem, and similarly, the presence of p40^{phox} did not modify the FRET level of the p67^{phox} tandem (Fig. 3*C* and Fig. S2), showing that in both cases, the overall geometry of the tandem is not significantly modified upon interaction with their partners.

FRET signals indicate specific interaction between p67^{phox} and p47^{phox} and provide information on their spatial organisation

The bi-molecular interaction between FP-tagged cytosolic subunits was then investigated using similar FLIM-FRET methodologies (Fig. 4). First, we studied the interaction of p67^{phox} and p47^{phox} (Fig. 4*A*, *B*, *C* and *F)*. Upon co-expression of p47^{phox}-CFP / p67^{phox}-YFP, the lifetimes of the CFP donor were on average significantly shorter than the reference value for p47^{phox}-CFP alone (Fig. 4*A* & 4*B*). However, as usual in dual expression systems, FRET efficiencies E_{app} varied strongly from cell to cell, depending on the amount of expressed acceptor. We thus determined E_{app} as a function of the acceptor quantity, as estimated from its average fluorescence intensity (Fig. 4*C*), or as a function of the ratio [A]/[D] (Fig. 4*F*), using a custom calibration procedure (see *SI*), as shown by others (14,15). In all cases, the FRET efficiency increases with the absolute or relative amount of acceptor.

For p47^{phox} and p67^{phox} subunits labeled at their C-termini (CC-labeling), E_{app} reaches a maximum value around 12 % at high acceptor levels (Fig. 4*C* & 4*F*). This is significantly higher than the negative control, consisting in the co-expression of p47^{phox}-CFP with YFP alone (Fig. 4*C* and Fig. S3*A*). As a second negative control, we used a truncated version of p47^{phox} missing the PRR domain (p47^{phox}ΔCter[1-342]) and leading *in vitro* to a complete abrogation of any interaction with p67^{phox} (16). The co-expression of p47^{phox}ΔCter-CFP with p67^{phox}-YFP gives clearly different FLIM images as compared to p47^{phox}-CFP, with well separated average lifetime distributions (Fig. 4*A* and 4*B*), and measured E_{app} values in the range of the first negative control (Fig. 4*C* and Fig. S3*A*). The observation of a plateau value for E_{app}, well above the values of the controls, provides a strong evidence for a specific interaction (17). The absence of significant FRET in the case of p47^{phox}ΔCter shows in addition that the PRR domain of p47^{phox} is required for this interaction in live cells.

We then modified the labeling sites of our FP tags, either by switching them to the N-termini or by exchanging FP colors between p47^{phox} and p67^{phox} (Fig. 4*C* & 4*F*). For the CN–tags, the maximum E_{app} of 8% was lower than for the CC-labeling (Fig. 4*F*), yet significantly above the negative controls (Fig. S3*A*). For the NN–tags, E_{app}, remained very low and close to the range of the negative controls (Fig. 4*C* and Fig. S3*A*).

To evaluate independently the occurrence of an interaction between p47^{phox} and p67^{phox} tagged at their N-termini, we used fluorescence cross-correlation spectroscopy (FCCS). In this technique, the fluctuations of the fluorescence intensities of FP-tagged p47^{phox} and p67^{phox} diffusing in and out a confocal volume in the cytosol of COS7 cells are analyzed by auto- and cross-correlation functions (see Experimental Procedure). A cross-correlation function with a non-null amplitude was observed for p47^{phox} and p67^{phox} tagged either at their CC and NN-termini (Fig. 5*A*), showing in both cases a co-diffusion of the fluorophores indicative of complex formation.

We thus observe a specific interaction between p47^{phox} and p67^{phox} cytosolic subunits for all tested positions and types of FP–tags, with in most cases E_{app} well above negative controls. Apparent FRET efficiencies measured in living cells are very complex average quantities. In addition, the efficiency of energy transfer depends on both the distance and relative orientation between the donor and the acceptor, as predicted by Förster theory (see Experimental Procedure). As the fluorescent proteins are attached to the subunits through variable flexible linkers (Table S1), a large range of relative FP orientations are likely allowed, leading to some averaging of the orientation factor. In the frame of this paper, we will thus assume that major differences in FRET efficiencies are chiefly governed by distance. This is supported by the similar FRET efficiencies observed when different D/A pairs are used, or when the anchoring sites of donor and acceptor are swapped (see for example Fig. 4*C* & 4*F)*.In this frame, the relative FRET efficiencies observed for donor and acceptor located at different termini provide interesting topological information. The maximum apparent FRET efficiency is higher for the CC–labeling than for the CN–labeling (Fig. 4*F*). Indeed, the two C termini are known to bind to each other and should be closer than the N-terminus of p67^{phox} and the C-terminus of p47^{phox}, which are separated by p67^{phox} itself (Fig. 1). For the NN–labeling, the distance between FPs is most likely too large to observe FRET, as we have evidence for complex formation through FCCS. The upper distance limit for a FRET-positive situation is about twice the Förster radius of the FRET pair (see experimental procedures), *c.a*. 100 Å. To fulfill this distance

Accepted manuscript

condition, the N–termini of both subunits should point to opposite directions in the complex.

FRET signals indicate specific interactions between p40^{phox} and p67^{phox}, and between p40^{phox} and p47^{phox}

We studied similarly the interactions between FP-tagged p40^{phox} and p67^{phox} (Fig. 4*D* and *G*, Fig. S3*B*). For all tag positions (NC, NN, or CC), specific FRET was observed with the same maximum efficiency around 8% at the plateau (Fig. 4*D* & 4*G*). The similar maximum FRET efficiencies indicate comparable distances between the different termini of p40^{phox} and p67^{phox}.

The direct p40^{phox}-p47^{phox} interaction was questioned to be of physiological relevance or to be rather an artificial phenomenon resulting from test tube experiments in the absence of p67^{phox} (4). The possible interaction sites were identified *in vitro* to be the SH3 domain of p40^{phox} and the C-terminal PRR domain of p47^{phox}, which is also the binding site for p67^{phox} (Fig. 1). We co-expressed p40^{phox} and p47^{phox} or its truncated version p47^{phox}ΔCter with NC or CC labeling (Fig. 4*E* and 4*H*). We found specific FRET in both cases with equivalent E_{app}, which indicates that the FP-tags at both termini of p40^{phox} have a similar average geometry relative to the C-terminus of p47^{phox}. When p47^{phox}ΔCter was used instead of full-length p47^{phox}, no significant FRET was observed (Fig. 4*E* and Fig. S3*C*). This confirms the requirement of the PRR domain of p47^{phox} for the interaction with p40^{phox} in live cells.

The cytosolic complex has a 1:1:1 composition with a high affinity between the subunits

FRET depends strongly on the number of acceptors in the direct vicinity of the donor and thus allows to explore the stoichiometry of the interaction (18). An uneven stoichiometry of the subunits in the complex (X : Y) will result in different maximum E_{app} when the donor and acceptor are swapped between subunits (Fig. S4). In contrast, even subunit ratios (X : X) will give the same maximum E_{app}. On hetero-dimers formed by p47^{phox} / p67^{phox} as well as by p40^{phox} / p67^{phox} , swapping donor and acceptor did not change the maximum apparent FRET efficiency (Fig. 4*F* and 4*G*). We also investigated possible homo-dimerization of the cytosolic subunits by co-expressing each subunit tagged with donor and acceptor FPs in the same cell. In all cases, the E_{app} scatters in the range of the negative controls (Fig. S5), indicating that there are no detectable homo-dimers. Taken together, our findings support a 1:1:1 stoichiometry for the cytosolic complex in the living cell, in agreement with in vitro experiments (19,20).

The amplitudes of the auto- and cross-correlation functions obtained by FCCS provide an estimate of the relative expression levels of the FP tagged subunits, and of their fraction in interaction (Experimental Procedures and SI). The FCCS analysis gives qualitatively similar results with FRET-positive CC-labeling or FRET-negative NN-labeling (Fig. 5*B*). In both cases, the fraction of interacting protein is correlated to the relative expression level of the proteins. While all p67^{phox} is bound in complex in the presence of a twofold excess of p47^{phox}, the fraction of p47^{phox} interacting with p67^{phox} decreases concomitantly. The apparent fraction of molecules in interaction is somewhat lower for the FRET-positive CC-labeling than for the FRET-negative NN-labeling, which may be ascribed to a FRET-induced decrease of the amplitude of the cross-correlation function (21).

The concentration of bound and free diffusing p47^{phox} and p67^{phox} obtained from the FCCS measurement can also be used to estimate their apparent dissociation constant, K_D^{app} (see *SI*). The median K_D^{app} value is in the range of a few hundred nM, showing a high affinity between p47^{phox} and p67^{phox} in live cells. Such a high affinity, with a K_D well below 1 µM, is consistent with previous values obtained *in vitro* ranging from 4 to 32 nM (22).

In conclusion, FRET imaging and FCCS experiments in live cells clearly demonstrate specific interactions between the three cytosolic subunits of the NADPH oxidase and give new insights into their spatial organization in the complexes. In the next paragraphs, we will use this information, together with SAXS, NMR and X-ray crystallography data to build a 3D model of the hetero-trimer. The crystallographic structure of p40^{phox} was solved (5) but p47^{phox} and p67^{phox} are highly flexible and only some domains were crystallized. First, we will describe how several putative conformations of p67^{phox} and p47^{phox} were selected from SAXS experiments. Second, we will assemble the individual subunits and choose along this process the most appropriate conformation of p47^{phox} and p67^{phox}, with the help of the topological information obtained from FRET, to finally propose a 3D model of the hetero-trimer compatible with our live cell experiments, as well as structural and biochemical results available in the literature.

Sets of models for p67^{phox} and p47^{phox} based on SAXS experiments

SAXS analysis consists in producing a set of atomic models compatible with the experimental SAXS curves using existing high-resolution structures of the crystallized domains,

Accepted manuscript

as explained in the section Experimental Procedures. For p67^{phox}, we re-examined previous experimental SAXS results (23) while new experiments were performed for the truncated p47^{phox}ΔCter [1-342] and for p47^{phox} to improve the model previously proposed by Durand et al. (24). For each of the three proteins, we retained a representative selection of possible models, that are discussed in the following steps.

The representative models of p47^{phox}ΔCter [1-342] were first examined in order to find a model adopting a relative orientation of its PX domain with the SH3 domains compatible with all other previous experimental observations (Fig. S6). First, in the resting state, p47^{phox} adopts an autoinhibited conformation in which the residues of the PX domain that interact with membrane phospholipids during the active phase are poorly accessible (25). Most of the models were rejected using this criterion (Fig. S6*A*, S6*B*). Second, the PX domain interacts with the lateral surface of N-terminal SH3 domain including Arg162 and Asp166 (16,25). Therefore, the latter two residues have to be located at the interaction surface between PX and SH3 domains (Fig. S6*C*). Third, previous kinetic analysis of H/D exchange coupled to mass spectrometry (HDX-MS) identified the residues involved in the intramolecular interaction in the resting state of p47^{phox}, which should also be masked (16).

We finally retained one model of p47^{phox} ΔCter that corresponds to all these criteria (Fig. 6*C*). The SAXS curve calculated on this model using the program CRYSOL is shown in Fig. 6*A* together with the experimental data (26). This model of truncated p47^{phox} was then used as starting point for the fit of the experimental SAXS pattern of the full-length p47^{phox} protein (Fig. 6*B*, Table S4), resulting in a set of full-length models carrying a mainly unstructured C-terminal part. Representative models of the full-length p47^{phox} protein were selected to build the whole 3D model of the hetero-trimer in the next section.

Step by step assembly of a 3D model of the NADPH oxidase cytosolic complex

Assuming a 1:1:1 stoichiometry, the representative SAXS models of full length p47^{phox} and p67^{phox} selected above, and the crystal structure of p40^{phox} were then used to build a model of the hetero-trimer, following a step by step workflow presented in Fig. S7. We know that p40^{phox} and p67^{phox} interact *via* their PB1 domains (Fig. 1) and the crystal structure of the p40^{phox}-PB1/ p67^{phox} –PB1 interaction has been solved (27). This was used as a template to add first the whole crystal structure of p40^{phox} onto p67^{phox} –PB1 (5) (Step I in Fig. S7). Then we added on the p67^{phox}-PB1 domain the full length p67^{phox} structural models previously selected. We selected the most appropriate model based on the following criteria, illustrated in Fig. S8. First, we kept the models that had neither clashes nor sterical hindrance with p40^{phox}. Second, considering the maximum dimension of p67^{phox} determined by SAXS (D_{max}~160 Å, Table S4) (23,28) and moreover the observation of significant FRET between the two termini of p67^{phox} in the p67^{phox} tandem, the N-terminus of p67^{phox} has to be bent toward its C-terminus. Third, for the p40^{phox} / p67^{phox} interaction, the significant and comparable FRET efficiencies for all tag positions (Fig. 4*G*) indicates that the termini of p40^{phox} and of p67^{phox} are at similar distances, and significantly below the maximum FRET-compatible distance of 100 Å. The later condition is only fulfilled when p40^{phox} and p67^{phox} adopt a cross-like spatial arrangement (Fig. S8). A representative p67^{phox} SAXS model compatible with all three criteria was selected (Step II in Fig. S7).

The resulting model of the p40^{phox} / p67^{phox} complex became the starting point to add p47^{phox}. The full length p47^{phox} SAXS models were added with the help of the NMR structure of the interaction between the C-termini of p47^{phox} and p67^{phox}, that are bound *via* their PRR (p47^{phox}) and SH3 (p67^{phox}) domains (29) (Step III in Fig. S7). Most of our full-length p47^{phox} SAXS models lead to steric clashes with p40^{phox} and/or a distance between the N-termini of p47^{phox} and p67^{phox} that is too short to account for the absence of clear FRET observed for NN-labeling of these two subunits (Fig. S9). This leads to the selection of a p47^{phox} SAXS model where p47^{phox} points in the opposite direction of p67^{phox} in a tail-to-tail orientation. This last step results in the complete 3D-model of the p40^{phox} / p47^{phox} / p67^{phox} hetero-trimer (step IV in Fig. S7 and Fig. 7).

Evaluation of our proposed 3D model : significant features and consistency with experimental data

Our assembled model of the NADPH oxidase cytosolic complex reveals an elongated structure where functional domains are connected by flexible peptide linkers (Fig. 7). As already stated, the proposed cross-like arrangement of p40^{phox} and p67^{phox} leads to distances between their termini compatible with significant and equivalent FRET for all combinations (Fig. 7*A*). The interaction of p47^{phox} with p67^{phox} also brings their C-termini in close vicinity, coherent with the high E_{app} measured for CC labeling, while the intermediate C-N distances are consistent with a lower E_{app} for the CN labelling (Fig. 7*B*).

Accepted manuscript

Interestingly, the FRET efficiency for the CN-tagged subunits is close to the one of the p67^{phox} tandem. Indeed, the C-termini of p47^{phox} and p67^{phox} are very close and separated from the N-terminus of p67^{phox} by a portion of p67^{phox} itself. On the other hand, p47^{phox} is expected to be elongated alone in solution (D_{max} by SAXS is in the order of 125 Å, Table S4) but the presence of intramolecular FRET in p47^{phox} tandems in live cells suggests that the subunit can adopt a more compact conformation. Indeed, the flexibility of its unstructured C-terminus clearly allows movements of the N-terminal domain (featured by an arrow in Fig. 7*C*). The absence of FRET between NN-labelled p47^{phox} and p67^{phox}, suggests that p47^{phox} cannot flip completely towards p67^{phox} but might adopt either a more elongated or more condensed conformations, as well as different angles with respect to the long axis of p67^{phox}. Our model should thus be viewed as a relatively flexible structure with significant variability around its multiple hinges. The D_{max} values of p67^{phox} and the p67^{phox} / p40^{phox} complex are close (Table S2). The D_{max} values of p67^{phox}-p47^{phox} and p67^{phox}-p47^{phox}-p40^{phox} are similar as well (Table S2). This means that the presence of p40^{phox} does not change the overall dimensions of the complex. This is again consistent with the cross-like spatial arrangement of p40^{phox} with p67^{phox} and with the observation of the same E_{app} of the p67^{phox} tandem with or without p40^{phox}. Finally, we find that the calculated SAXS curves using the program CRYSOL on the p67^{phox} - p47^{phox} - p40^{phox} model is in reasonable agreement with the experimental curves published by Yuzawa et al. (Fig. S10) (28).

Discussion

Here we presented an integrated workflow to analyze the intermolecular interactions and the conformation of a complex of proteins formed by structured domains separated by unstructured segments in living cells. This analytical strategy may be adapted to any cytosolic protein complex composed of partially disordered subunits.

We first demonstrate the complementarity of FRET-FLIM and FCCS to characterize live cell interactions, estimate binding affinity and obtain topological information using the same FP-labeling for both techniques. This was made possible owing to the new cyan variants mTurquoise and Aquamarine in the classical CFP/YFP FRET pair (7). Their increased brightness and photostability allowed both improved performances as donors for FLIM and full suitability for two-color FCCS experiments.

The dynamic NADPH oxidase complex depends on protein assembly for activation, and thus the development of inhibitors of this assembly is an attractive concept to regulate its activity (30,31). For the p40^{phox}-p47^{phox}-p67^{phox} complex, there is a discrepancy between the 1:1:1 stoichiometry found in *in vitro* experiments (19,20) and the 2 – 3 times higher expression level of p47^{phox} in comparison to p67^{phox} in neutrophils (32). In addition, this higher amount of p47^{phox} compared to p67^{phox} implies that p47^{phox} is present both as a free and complex-bound subunit (32). However, it is not known whether free p67^{phox} exists. Our results revealed two pairwise interactions with a one to one stoichiometry, p47^{phox} / p67^{phox} and p40^{phox} / p67^{phox} that strongly suggest that the ternary complex is assembled in a 1:1:1 stoichiometry inside a live cell. Furthermore, in the presence of an excess of p47^{phox}, all p67^{phox} were bound in complex. In solution, about 10 % to 20 % of recombinant p47^{phox} and p67^{phox} proteins have been detected as dimers (22). We did not observe any dimers by FRET-FLIM. Indeed, in live cells, the unbound cytosolic subunits may encounter a large diversity of potential partners that likely limits dimer formation.

Our live cell FRET results also provide topological information that nicely complements structural data from X-ray crystallography, NMR and SAXS experiments obtained on purified recombinant proteins. The combination of SAXS data and single-molecule FRET *in vitro* is very useful to investigate protein-folding by integrating complementary information (33-35). The combination of SAXS with FRET measurements of FP-labelled proteins *in cellulo* provides lower spatial and temporal resolution, however it affords access to the conditions in living cells. To our knowledge, such an approach has not been described before. These pieces of information were integrated to build a new model of the cytosolic NADPH oxidase complex with several noticeable features: (i) p47^{phox} and p67^{phox} interact via their C-termini in a tail-to-tail configuration. Their N-termini are over 100 Å apart, (ii) p67^{phox} and p47^{phox} are not fully elongated and (iii) p40^{phox} and p67^{phox} adopt a cross-like conformation (Fig. 7). The model is consistent with the idea that p47^{phox} is required for the initial assembly of the functional oxidase. Indeed, the PX-domain and the SH3 domains of p47^{phox} are located on one end of the complex, ideally positioned to interact with phospholipids (PX-domain) and with p22^{phox} (SH3 domains) to initiate oxidase assembly. This may then bring p40^{phox} and p67^{phox} closer to the membrane. Indeed, the PX-domain of p40^{phox} also interacts with membrane lipids and the N-terminus of p67^{phox} requires several activation steps mandatory for superoxide production. The flexible hinge between the N-terminal half of p47^{phox} and the rest of the trimeric complex may be required to establish the initial contact with phospholipids

Accepted manuscript

and $p22^{phox}$ and then bend the complex to bring $p67^{phox}$ closer to Nox2. In addition, the proximity of the C-terminus of $p47^{phox}$ with the SH3 domain of $p40^{phox}$ in the model raises the question whether $p40^{phox}$ contributes to stabilize the C-terminus of $p47^{phox}$ at the SH3 domain of $p67^{phox}$. The position of the $p40^{phox}$ PX domain in the middle of the elongated complex is unfavorable for a role of this domain in the initiation of oxidase assembly since it would require a lateral attachment of the complex on the membrane. However, if $p47^{phox}$ leaves the active complex as recently suggested (36), the $p40^{phox}$ PX domain would be in a favorable position to bind to phosphoinositides in the membrane after its dissociation from PB1 (5) and this would help keeping $p67^{phox}$ in place (37).

In $p67^{phox}$, the TPR and the activation domain are essential for the assembly with Rac and Nox2 and, ultimately, for activation of the oxidase. In the proposed model of the hetero-trimer, presented here in the resting state (Fig. 7), the N-terminal region of $p67^{phox}$ is well exposed and accessible. We assume that the global orientation and the internal flexibility between its domains is fully compatible with the binding to Rac or to Nox2 trough the activation domain (38). At this stage of characterization of the ternary cytosolic complex, it seems that the main limiting step towards activation is $p47^{phox}$ that needs to be activated to promote assembly of the whole cytosolic complex at the membrane. Preventing the conformational changes of the N-terminus of $p47^{phox}$ would probably block the subsequent interactions with the membrane and $p22^{phox}$ and prevent oxidase activation. Therefore, our approach provides critical information for the design of inhibitors that would interfere with key steps in the activation process. Furthermore, the data we obtained and the model are a starting point to investigate the changes that may occur during activation of the oxidase. They may also serve to compare wild-type subunits with mutations found in patients with chronic granulomatous disease in order to understand the phenotype of this oxidase deficiency.

Experimental procedures

Plasmid library and transfection. Plasmids encoding full length human $p47^{phox}$ (NCF1) and $p67^{phox}$ (NCF2) both embedded in a pEGFP-N1 vector (Clontech) (36), and $p40^{phox}$ (NCF4) embedded in a CMD8 vector (Gift from Marie Claire Dagher) were used as a starting point to build a full library of N- and C-terminal tagged fusion proteins. The cDNA of the subunits were cut out with restriction enzymes or amplified by PCR and inserted in either cyan mTurquoise or Aquamarine-N1 or –C1 vectors (variants of the pECFP vectors: mTurquoise: T65S-S72A-H148D-S175G-A206K (39), Aquamarine: T65S, H148G (40)), yellow Citrine-N1 or –C1 vectors (the mutation Q69M was introduced into EYFP) (8), or the red mCherry-C1 vector (Clontech, Takara Biotechnology, Co., Ltd). The internal start codon (ATG) was removed by PCR from the FP-N1 vectors or from the subunits embedded in FP-C1 vectors. Table S1 displays an overview of the constructs. In order to build the plasmids coding for RFP-2A-$p67^{phox}$ or $p40^{phox}$, we ordered a synthetic gene coding for mCherry-P2A (P2A=ATNFSLLKQAGDVEENPGP) (12) framed by AgeI and HindIII restriction sites (Eurofins). The two enzymes were used to cut out the FP and insert mCherry-2A in pECitrine-p67-C1 or pEmCherry-p40-C1. Primers were purchased from Eurogentec (Kaneka corp., Japan). Plasmids were amplified in DH5α *Escherichia coli*, DNA was purified with E.N.Z.A. ® mini kit 2 (Omega Bio.Tek). For transfection, cells (COS7 or $COS^{Nox2/\ p22}$) were seeded either on glass coverslips (Ø 25 mm, thickness 0.13 – 0.16 mm) in 6-well plates for microscopy or in 24-well plates for luminometry one day before the experiment. Cells were transiently transfected with XtremeGene HP (Roche Diagnostics) following the supplier's instructions and used 24 – 48 h after transfection. Transfection efficiency, monitored by flow cytometry, was constantly between 20 – 30 % for triple transfection. Based on the high reproducibility of transfection efficiencies, we assumed that the subunits without FP-tag were present in the cells at the same average level as the FP-tagged ones.

Cell culture. COS7 cells were purchased from ATCC and cultured following the supplier's instructions. COS7 cells stably expressing Nox2 and $p22^{phox}$ ($COS^{Nox2/\ p22}$) were kindly provided by M. Dinauer (Washington University School of Medicine, St. Louis, MO) and cultured in medium containing selecting antibiotics (10).

$O_2^{\bullet-}$ detection by L-012 chemiluminescence. L-012 (100 µM Wako Chemicals) and HRP (20 U/ml) were mixed and added to the well containing transfected $COS^{Nox2/\ p22}$ cells a few minutes before the addition of 500 nM of PMA to stimulate the assembly of the NADPH oxidase. 20 µM of DPI was added to stop the $O_2^{\bullet-}$ production. The production was quantified as the relative light units (RLU) area under the curve recorded during 30 mins with a SynergyH1 plate reader (Biotek, USA).

Accepted manuscript

Fluorescence Lifetime Imaging Microscopy (FLIM). Time resolved laser scanning TCSPC microscopy was performed on a custom made microscope as described previously (40). Briefly, the setup is based on a TE2000 microscope with a 60x, 1.2NA water immersion objective (Nikon). The epifluorescence pathway is equipped with an Hg lamp, a set of filter cubes for the different FPs and a CCD camera (ORCA-AG, Hamamastu Photonics, Table S3). The TCSPC path is equipped with pulsed laser diodes (440 nm for CFPs; 466 nm for YFPs, PicoQuant) driven by a PDL800 driver (20 MHz, PicoQuant). The C1 scanning head (Nikon) probes a 100 x 100 µm maximum field of view. To select the FP fluorescence, dichroic mirrors (DM) and filter sets were used before the detection by a MCP-PMT detector (Hamamatsu Photonics). The signals were amplified by a fast pulse pre-amplifier (Phillips Scientific) before reaching the PicoHarp300 TCSPC module (PicoQuant). Counting rates were routinely between 50 000 and 100 000 cts/s. Transfected cells were kept in PBS at 20°C and studied for 2 h maximum in an Attofluor cell chamber (Thermo Fisher Scientific).

The lifetime of a fluorophore is an intensive property, independent of its concentration, which can be precisely monitored even in live cells. A precision of a few percent on lifetime is common (17,41,42,43 ,44). The TCSPC fluorescence decay of all the pixels of the cytosol was computed by the SymPhoTime software (Fig. 3*A*). The decays were fitted with a mono-exponential fit function (Eq. 1a) for the control cells expressing a donor-fusion protein (without acceptor), the donor being Aquamarine, mTurquoise and Citrine (Fig. 3*A*, left).

$$I(t) = I_0\, e^{-\frac{t}{\tau_{donor}}} + C, \qquad \textbf{[1a]}$$

where C is the constant background.As the donor has a mono-exponential lifetime, its fluorescence decay in the presence of FRET to an acceptor can be fitted with a bi-exponential function (Eq. 1b, Fig. 3*A*, right).

$$I(t) = \alpha_{long}\, I_0\, e^{-\frac{t}{\tau_{long}}} + \alpha_{short}\, I_0\, e^{-\frac{t}{\tau_{short}}} + C, \qquad \textbf{[1b]}$$

where C is the constant background. α_{long} and α_{short} are the proportions of a long (τ_{long}) and a short (τ_{short}) lifetime component respectively. For fitting, we used a custom made procedure in IGOR Pro (WaveMetrics). The quality of the fits is evaluated by the weighted residual distribution and Pearson's χ^2 test (Fig. 3*A*).

$< \tau_{DA} >$ is the average lifetime of the donor-fusion protein, D, in presence of an acceptor-fusion protein, A, (Eq. **2**):

$$< \tau_{DA} >= \alpha_{long}\tau_{long} + \alpha_{short}\tau_{short} \qquad \textbf{[2]}$$

The apparent FRET efficiency E_{app} is calculated using $< \tau_{DA} >$ and τ_{Donor} (Eq. 3):

$$E_{app} = 1 - \frac{<\tau_{DA}>}{\tau_{Donor}} \times 100 \qquad \textbf{[3]}$$

It was calculated on a cell by cell basis from the fluorescence decays obtained for each cell using for τ_{Donor} the lifetime of the same donor/subunit fusion protein alone.

The apparent FRET efficiencies measured in each cell are complex averages over highly heterogeneous populations of donor molecules engaged in different FRET interactions. Fundamentally, these FRET efficiencies depend on both the distance and relative orientation between donor and acceptor. The determination of distances between FRET partners thus requires some assumption on the orientation factor κ^2 (45). Unfortunately, the *dynamic* isotropic regime leading to the popular value $\kappa^2=2/3$ cannot be applied to fluorescent proteins, since their rotational correlation time in water is around 14 ns *i.e.* three to four times longer than the lifetime of the donor excited state (46 ,47). In the viscous environment of living cells, FPs must be considered as *static* on the time scale of the FRET interaction. On the other hand, since FPs are fused to the subunits through flexible linkers, they are expected to adopt a whole set of conformations, leading to broadly distributed, but probably non-isotropic and non-homogeneous relative orientations and distances. Therefore, the precise calculation of distances from our FRET data, as proposed for example by Vogel et al (48), is mostly out of reach. Instead, we used the apparent FRET efficiencies to establish distance limits, to guide topological reasoning or to provide comparative information. Indeed, whatever the effective value of κ^2, the observation of a significant FRET indicates some proximity within the range of the critical Förster distance R°. Typical Förster distances of most fluorescent protein FRET pairs, calculated using $\kappa^2=2/3$, lie in the range of 50-60 Å (48). R° evolves as $(\kappa^2)^{1/6}$ and thus varies only slowly with the orientation factor. Using $\kappa^2=0.476$, a value applicable to fully isotropic and homogeneous static averaging (17,45,49), we obtain quite similar values of R°= 57 Å for Aquamarine / Citrine and 55 Å for Citrine / mCherry. For the maximum, but highly unlikely value $\kappa^2=4$, these distances would at most extend to 81 Å and 78 Å respectively. In cases of unfavorable relative orientations, R° could on the contrary decrease significantly below 50 Å. Conversely, as the D/A distance approaches twice R°, the FRET efficiency will tend virtually to 0. As a rule of thumb, assuming some degree of orientational and conformational averaging, and considering our practical detection limits, we took

Accepted manuscript

100 Å as the upper distance limit to observe FRET in this study.

The FP-tagged subunits are transiently expressed and the level of expression may strongly vary between cells. We recorded intensity images before any FLIM experiments on the same field of view. The intracellular concentrations are proportional to the average fluorescence intensities. E_{app} was commonly plotted as a function of the fluorescence intensity of the acceptor in the cell, *I(A)* to observe a FRET-positive situation (17,50-53). As a negative control, the donor/subunit fusion protein was co-expressed with the free acceptor. This control is useful to (i) determine if E_{app} is significant and (ii) to set the threshold for the maximum value of *I(A)* beyond which unspecific FRET due to molecular crowding starts to contribute to the signals. Indeed, when the cells are crowded with the acceptors, *I(A)* becomes very high and the donors show unspecific FRET with the acceptors nearby just because of the spatial proximity (17). We discarded such cells.

The plotting of E_{app} against $[A]/[D]$ required the calibration of fluorescence intensities measured in both donor and acceptor channel. The ratio of fluorescence intensities, $I(A)/I(D)$, was transformed in the concentration ratio of fluorescent proteins, $[A]/[D]$, using a custom calibration procedure of the microscopy setup (see *SI*).

Fluorescence Cross Correlation Spectroscopy. A confocal microscope Leica TCS SP8 SMD (Leica Microsystems) was used. It is equipped with a DMI 6000 CS stand and a 63x/1.2 HC PL APO water immersion objective, a continuous argon laser (514 nm from Leica TCS SP8) and a diode pulsed laser (440 nm, PicoQuant). The signal was selected by 505 nm DM and two bandpass filters (BP 478/22, BP 540/30) and detected by two APD detectors (PicoQuant). For the detection, the SMD module is constituted of a PicoHarp3000 system for TTTR mode of single photon counting (PicoQuant). Cells were kept in an air-conditioned chamber at 30°C. In order to correct for the crosstalk between the CFP and YFP detection channels on the amplitudes of the correlation functions, we used a variant of fluorescence correlation spectroscopy called fluorescence lifetime correlation spectroscopy (FLCS) (54). The fluorescence signal of each channel was corrected from spectral bleed-through using FLCS filters as described elsewhere (55,56). In this method combining TCSPC and FCS, the different FCS contributions are separated by using the different fluorescence decay pattern of both fluorophores. The fluctuations of fluorescence intensity were auto- and cross-correlated and the resulting curves were analyzed using a standard pure diffusion model with SymphoTime (PicoQuant).

The auto-correlation function of fluorescence fluctuations returns the time needed for the fluorophore to cross the confocal observation volume, V_{FP}, and the number of molecules, N_{FP}, present in V_{FP}. N_{FP} is the inverse of the amplitude to the auto-correlation function, $G_{FP}(0)$ (21). The concentrations of FPs in the observation volume are calculated as following where N_A is the Avogadro number (Eq. 4):

$$[YFP] = \frac{1}{G_{YFP}(0)}\frac{1}{N_A}\frac{1}{V_{YFP}}, [CFP] = \frac{1}{G_{CFP}(0)}\frac{1}{N_A}\frac{1}{V_{CFP}} \quad \textbf{[4]}$$

The amplitude of the cross-correlation function, $G_{cross}(0)$, allows the estimation of the concentration of the stoichiometric p47^{phox}-p67^{phox} complex. p47^{phox} and p67^{phox} are respectively labelled with YFP and CFP (Eq. 5).

$$[Complex] = \frac{G_{cross}(0)}{G_{YFP}(0)\cdot G_{CFP}(0)}\frac{1}{N_A}\frac{1}{V_{cross}} \quad \textbf{[5]}$$

In practice, the observation volumes in the two channels, V_{YFP} and V_{CFP}, and V_{cross} have always different sizes and are not perfectly coincident. In addition, a fraction of FPs might be non-fluorescent due to non-matured protein, dark state or photobleaching (21). The later was kept here below 10%. In order to minimize the impact of these limits on the detection of interactions, the fractions, X, of co-diffusing fluorophores that are also the fractions of protein in interaction, were normalized to the average fractions obtained for the p67^{phox} tandem, whose two tags diffuse together (Eq. 6).

$$X_{YFP}^{cplx} = \frac{G_{cross}(0)}{G_{CFP}(0)}\left\langle\frac{G_{CFP}^{tandem}(0)}{G_{cross}^{tandem}(0)}\right\rangle \times 100 \quad \textbf{[6]}$$

$$X_{CFP}^{cplx} = \frac{G_{cross}(0)}{G_{YFP}(0)}\left\langle\frac{G_{YFP}^{tandem}(0)}{G_{cross}^{tandem}(0)}\right\rangle \times 100 \quad \textbf{[6]}$$

In addition, the relative amount of both partners was estimated as (Eq. 7):

$$\frac{[YFP]^{cplx}}{[CFP]^{cplx}} = \frac{G_{CFP}(0)}{G_{YFP}(0)} \times \left\langle\frac{G_{YFP}^{tandem}(0)}{G_{CFP}^{tandem}(0)}\right\rangle \quad \textbf{[7]}$$

The details for the computation of K_D^{app} can be found in *SI*.

Protein preparation, SAXS data acquisition and processing. p47^{phox} constructs were expressed as a GST fusion protein using a pGex-6P-1 derived vector containing the cDNA corresponding to the full amino acids sequence (from 1 to 397) for the full length p47^{phox} or to a sequence coding for amino acids 1 to 342 for the p47^{phox}ΔCter construct lacking the C-terminal end of the protein after the AIR motif. For both constructs, the production protocol was the same. The proteins were expressed in *E. coli*, strain BL21(DE3). Expression was induced with 0.5 mM IPTG, when the cell culture reached an OD of

Accepted manuscript

0.6 at 600 nm. Temperature was then shifted to 20°C for an overnight induction. Cells were harvested and resuspended in chilled lysis buffer (50 mM Tris, pH 7.5, 0.3 M NaCl, 1 mM EDTA, 2 mM DTT and Complete EDTA-free protease inhibitor (Roche Diagnostics, Basel, Switzerland)). All following operations were carried out at 4°C. Cells were disrupted by sonication, then centrifuged at 40 000 rpm for 40 min in a Beckman 45 Ti rotor. The supernatant was loaded onto a 4 mL Gluthation-Sepharose 4B column (GE Healthcare) equilibrated in the lysis buffer. Proteins were eluted at 1 mL/min with 50 mL of elution buffer (50 mM Tris, pH 7.5, 50 mM NaCl, and 10 mM Glutathion). Fractions containing GST fusion of the corresponding $p47^{phox}$ construct were pooled and digested overnight at 4°C with PreScission protease (70 units enz. per 40 mg of protein). Due to the genetic construction, digested $p47^{phox}$ possesses 10 and 7 additional residues at its N- and C-terminus, respectively and $p47^{phox}$ΔCter only 10 additional residues at its N-terminus. Digestion products were loaded at a flow rate of 1 mL/min onto a MonoS column (GE Healthcare) equilibrated in 50 mM Hepes pH7.5, 50 mM NaCl, 1 mM EDTA, and 2 mM DTT. The proteins were eluted with a 40 mL linear gradient of NaCl (50-500 mM). The resulting protein fractions containing the corresponding $p47^{phox}$ construct were concentrated on a centrifugal concentration device with a 10 kDa cutoff. The protein was then diluted 20 times in Hepes 50 mM pH 7.5, 100 mM NaCl, 1 mM EDTA, 2 mM DTT, and 5% glycerol, and finally re-concentrated at different concentrations where aliquots of $p47^{phox}$, or $p47^{phox}$ΔCter, were taken and stored for SAXS measurements. For $p67^{phox}$, $p47^{phox}$ and its truncated version, SAXS data processing led to a molecular mass close to that derived from the sequence showing that the protein solutions were devoid of oligomers (Table S4).

SAXS measurements on $p47^{phox}$ΔCter were performed on a laboratory instrument Nanostar (Bruker Nanostar, $\lambda = 1.54$Å). SAXS data on $p47^{phox}$ full length were collected on the SWING beamline (SOLEIL synchrotron, St Aubin, $\lambda = 1.0$Å). Both proteins were studied at different concentrations (see Table S4). SAXS data were normalized to the intensity of the incident beam, averaged and background subtracted using the program package PRIMUS (57), intensities were put on an absolute scale using water scattering. The final pattern used for fitting was obtained by extrapolating to infinite dilution of the set of curves recorded at the different concentrations.

$p47^{phox}$ΔCter was modelled using the program BUNCH (58), which combines rigid-body and *ab initio* modelling approaches. The program starts from known structures of the two domains PX and SH3 tandem (PDB ID 1KQ6 and 1NG2, respectively) and finds the optimal positions and orientations of domains and probable conformations of the linkers by fitting the SAXS curve calculated on the model to the experimental curve. In a final step, we substituted the dummy residues of the linkers with all atom descriptions using the programs PD2 (59) and SCWRL4 (60). An ultimate adjustment was performed using the program CRYSOL. The modelling was repeated 100 times. Finally, models giving the best agreement with the experimental curve (lowest χ^2 values) were selected. The same approach was used for $p47^{phox}$ full length using the most probable model describing $p47^{phox}$ΔCter and the PRR domain (extracted from the PDB ID 1K4U) as starting point. Models of $p67^{phox}$ were built in the same way starting from the known structures (23). This modelling has shown than $p67^{phox}$ is able to adopt a great variety of very different conformations. Not surprisingly the SAXS data can be fitted using an ensemble of models (EOM approach). (61) All SAXS data are shown in SASBDB (https://www.sasbdb.org) under the SAS codes SASDEJ3, SASDEK3 and SASDEL3.

Molecular structure alignment. PDB structures and SAXS-based models were imported into the PyMOL Molecular Graphics System, Version 1.8 Schrödinger, LLC.

Statistical Analysis. Data are represented as means of at least three independent experiments ± SEM. Significance was tested with one-way ANOVA followed by a Tukey's Multiple Comparison Test using GraphPad Prism version 5.

Accepted manuscript

Acknowledgements: $COS^{Nox2/\ p22phox}$ cells were a kind gift from Marie Dinauer. This work has benefited from the flow cytometry facility SpICy and the Microscopy Rennes Imaging Centre (MRic) for FCS measurements. Cornelia Ziegler is a recipient of a doctoral grant from IDEX Paris-Saclay. Leïla Bouchab is a recipient of a doctoral grant from Region Île-de -France (DIM Malinf). This work was supported by a FRM grant (Fondation for medical research, DCM20121225747), by the LabEx PALM (ANR-10-LABX-0039-PALM) and by the IDEX Paris Saclay (IRS BioProbe). We thank Julien Marcoux for the preparation of proteins for the SAXS experiments, Sophie Sacquin-Mora and Antoine Taly for fruitful discussion. We thank the staff of the SWING beamline for help during the SAXS measurements.

Conflict of interest: The authors declare that they have no conflicts of interest with the contents of this article.

Accepted manuscript

References

1. Uversky, V. N. (2016) Dancing Protein Clouds: The Strange Biology and Chaotic Physics of Intrinsically Disordered Proteins. *J. Biol. Chem.* 291, 6681-6688
2. Pauwels, K., Lebrun, P., and Tompa, P. (2017) To be disordered or not to be disordered: is that still a question for proteins in the cell? *Cell. Mol. Life. Sci.* 74, 3185-3204
3. Sumimoto, H. (2008) Structure, regulation and evolution of Nox-family NADPH oxidases that produce reactive oxygen species. *FEBS J.* 275, 3249-3277
4. Massenet, C., Chenavas, S., Cohen-Addad, C., Dagher, M.-C., Brandolin, G., Pebay-Peyroula, E., and Fieschi, F. (2005) Effects of p47phox C Terminus Phosphorylations on Binding Interactions with p40phox and p67phox: structural and functional comparison of p40phox and p67phox SH3 domains. *J. Biol. Chem.* 280, 13752-13761
5. Honbou, K., Minakami, R., Yuzawa, S., Takeya, R., Suzuki, N. N., Kamakura, S., Sumimoto, H., and Inagaki, F. (2007) Full-length p40phox structure suggests a basis for regulation mechanism of its membrane binding. *EMBO J.* 26, 1176-1186
6. Piovesan, D., Tabaro, F., Paladin, L., Necci, M., Micetic, I., Camilloni, C., Davey, N., Dosztanyi, Z., Meszaros, B., Monzon, A. M., Parisi, G., Schad, E., Sormanni, P., Tompa, P., Vendruscolo, M., Vranken, W. F., and Tosatto, S. C. E. (2018) MobiDB 3.0: more annotations for intrinsic disorder, conformational diversity and interactions in proteins. *Nucleic Acids Res.* 46, D471-D476
7. Merola, F., Erard, M., Fredj, A., and Pasquier, H. (2016) Engineering fluorescent proteins towards ultimate performances: lessons from the newly developed cyan variants. *Methods Appl. Fluoresc.* 4: 012001
8. Griesbeck, O., Baird, G. S., Campbell, R. E., Zacharias, D. A., and Tsien, R. Y. (2001) Reducing the environmental sensitivity of yellow fluorescent protein. Mechanism and applications. *J. Biol. Chem.* 276, 29188-29194
9. Shaner, N. C., Campbell, R. E., Steinbach, P. A., Giepmans, B. N. G., Palmer, A. E., and Tsien, R. Y. (2004) Improved monomeric red, orange and yellow fluorescent proteins derived from Discosoma sp. red fluorescent protein. *Nat. Biotech.* 22, 1567-1572
10. Yu, L., Zhen, L., and Dinauer, M. C. (1997) Biosynthesis of the Phagocyte NADPH Oxidase Cytochromeb 558 : role of heme incorporation and heterodimer formation in maturation and stability of gp91phox and p22phox subunits. *J. Biol. Chem.* 272, 27288-27294
11. Betolngar, D.-B., Erard, M., Pasquier, H., Bousmah, Y., Diop-Sy, A., Guiot, E., Vincent, P., and Mérola, F. (2015) pH sensitivity of FRET reporters based on cyan and yellow fluorescent proteins. *Anal. Bioanal. Chem.* 407, 4183-4193
12. Kim, J. H., Lee, S.-R., Li, L.-H., Park, H.-J., Park, J.-H., Lee, K. Y., Kim, M.-K., Shin, B. A., and Choi, S.-Y. (2011) High Cleavage Efficiency of a 2A Peptide Derived from Porcine Teschovirus-1 in Human Cell Lines, Zebrafish and Mice. *PLoS ONE* 6, e18556
13. Goedhart, J., van Weeren, L., Adjobo-Hermans, M. J. W., Elzenaar, I., Hink, M. A., and Gadella, T. W. J., Jr. (2011) Quantitative Co-Expression of Proteins at the Single Cell Level – Application to a Multimeric FRET Sensor. *PLoS ONE* 6, e27321
14. Cardarelli, F., Bizzarri, R., Serresi, M., Albertazzi, L., and Beltram, F. (2009) Probing Nuclear Localization Signal-Importin α Binding Equilibria in Living Cells. *J. Biol. Chem.* 284, 36638-36646
15. Greife, A., Felekyan, S., Ma, Q. J., Gertzen, C. G. W., Spomer, L., Dimura, M., Peulen, T. O., Woehler, C., Haussinger, D., Gohlke, H., Keitel, V., and Seidel, C. A. M. (2016) Structural assemblies of the di- and oligomeric G-protein coupled receptor TGR5 in live cells: an MFIS-FRET and integrative modelling study. *Sci. Rep.* 6:36792
16. Marcoux, J., Man, P., Petit-Haertlein, I., Vives, C., Forest, E., and Fieschi, F. (2010) p47(phox) Molecular Activation for Assembly of the Neutrophil NADPH Oxidase Complex. *J. Biol. Chem.* 285, 28980-28990

Accepted manuscript

17. Grailhe, R., Merola, F., Ridard, J., Couvignou, S., Le Poupon, C., Changeux, J.-P., and Laguitton-Pasquier, H. (2006) Monitoring Protein Interactions in the Living Cell Through the Fluorescence Decays of the Cyan Fluorescent Protein. *ChemPhysChem* 7, 1442-1454
18. Vogel, S. S., Thaler, C., and Koushik, S. V. (2006) Fanciful FRET. *Sci. STKE* 331:re2
19. Stasia, M., and Li, X. (2008) Genetics and immunopathology of chronic granulomatous disease. *Semin. Immunopathol.* 30, 209-235
20. Nauseef, W. M. (2004) Assembly of the phagocyte NADPH oxidase. *Histochem. Cell Biol.* 122, 277-291
21. Foo, Yong H., Naredi-Rainer, N., Lamb, Don C., Ahmed, S., and Wohland, T. (2012) Factors Affecting the Quantification of Biomolecular Interactions by Fluorescence Cross-Correlation Spectroscopy. *Biophys. J.* 102, 1174-1183
22. Karimi, G., Houée Levin, C., Dagher, M. C., Baciou, L., and Bizouarn, T. (2014) Assembly of phagocyte NADPH oxidase: A concerted binding process? *BBA - Gen. Subjects* 1840, 3277-3283
23. Durand, D., Vivès, C., Cannella, D., Pérez, J., Pebay-Peyroula, E., Vachette, P., and Fieschi, F. (2010) NADPH oxidase activator p67phox behaves in solution as a multidomain protein with semi-flexible linkers. *J. Struct. Biol.* 169, 45-53
24. Durand, D., Cannella, D., Dubosclard, V., Pebay-Peyroula, E., Vachette, P., and Fieschi, F. (2006) Small-Angle X-ray Scattering Reveals an Extended Organization for the Autoinhibitory Resting State of the p47phox Modular Protein. *Biochemistry* 45, 7185-7193
25. Karathanassis, D., Stahelin, R. V., Bravo, J., Perisic, O., Pacold, C. M., Cho, W., and Williams, R. L. (2002) Binding of the PX domain of p47phox to phosphatidylinositol 3,4-bisphosphate and phosphatidic acid is masked by an intramolecular interaction. *EMBO J.* 21, 5057-5068
26. Svergun, D., Barberato, C., and Koch, M. H. J. (1995) CRYSOL - A program to evaluate x-ray solution scattering of biological macromolecules from atomic coordinates. *J. Appl. Crystallogr.* 28, 768-773
27. Wilson, M. I., Gill, D. J., Perisic, O., Quinn, M. T., and Williams, R. L. (2003) PB1 Domain-Mediated Heterodimerization in NADPH Oxidase and Signaling Complexes of Atypical Protein Kinase C with Par6 and p62. *Mol. Cell* 12, 39-50
28. Yuzawa, S., Miyano, K., Honbou, K., Inagaki, F., and Sumimoto, H. (2009) The domain organization of p67 phox, a protein required for activation of the superoxide-producing NADPH oxidase in phagocytes. *J. Innate Immun.* 1, 543-555
29. Kami, K., Takeya, R., Sumimoto, H., and Kohda, D. (2002) Diverse recognition of non-PxxP peptide ligands by the SH3 domains from p67phox, Grb2 and Pex13p. *EMBO J.* 21, 4268-4276
30. Cifuentes-Pagano, M. E., Meijles, D. N., and Pagano, P. J. (2015) Nox Inhibitors & Therapies: Rational Design of Peptidic and Small Molecule Inhibitors. *Curr. Pharm. Design* 21, 6023-6035
31. Laraia, L., McKenzie, G., Spring, D. R., Venkitaraman, A. R., and Huggins, D. J. (2015) Overcoming Chemical, Biological, and Computational Challenges in the Development of Inhibitors Targeting Protein-Protein Interactions. *Chem. Biol.* 22, 689-703
32. DeLeo, F. R., and Quinn, M. T. (1996) Assembly of the phagocyte NADPH oxidase: molecular interaction of oxidase proteins. *J. Leuk. Biol.* 60, 677-691
33. Boura, E., Różycki, B., Herrick, D. Z., Chung, H. S., Vecer, J., Eaton, W. A., Cafiso, D. S., Hummer, G., and Hurley, J. H. (2011) Solution structure of the ESCRT-I complex by small-angle X-ray scattering, EPR, and FRET spectroscopy. *PNAS* 108, 9437-9442
34. Fuertes, G., Banterle, N., Ruff, K. M., Chowdhury, A., Mercadante, D., Koehler, C., Kachala, M., Estrada Girona, G., Milles, S., Mishra, A., Onck, P. R., Grater, F., Esteban-Martin, S., Pappu, R. V., Svergun, D. I., and Lemke, E. A. (2017) Decoupling of size and shape fluctuations in heteropolymeric sequences reconciles discrepancies in SAXS vs. FRET measurements. *PNAS* 114, E6342-E6351

Accepted manuscript

35. Peti, W., Page, R., Boura, E., and Rozycki, B. (2018) Structures of Dynamic Protein Complexes: Hybrid Techniques to Study MAP Kinase Complexes and the ESCRT System. *Methods Mol. Biol.*, 1688, 375-389
36. Faure, M. C., Sulpice, J.-C., Delattre, M., Lavielle, M., Prigent, M., Cuif, M.-H., Melchior, C., Tschirhart, E., Nüße, O., and Dupré-Crochet, S. (2013) The recruitment of p47phox and Rac2G12V at the phagosome is transient and phosphatidylserine dependent. *Biol. Cell* 105, 501-518
37. Song, Z. M., Bouchab, L., Hudik, E., Le Bars, R., Nusse, O., and Dupre-Crochet, S. (2017) Phosphoinositol 3-phosphate acts as a timer for reactive oxygen species production in the phagosome. *J. Leuk. Biol.* 101, 1155-1168
38. Lapouge, K., Smith, S. J. M., Walker, P. A., Gamblin, S. J., Smerdon, S. J., and Rittinger, K. (2000) Structure of the TPR Domain of p67phox in Complex with Rac·GTP. *Mol. Cell* 6, 899-907
39. Goedhart, J., van Weeren, L., Hink, M. A., Vischer, N. O. E., Jalink, K., and Gadella, T. W. J. (2010) Bright cyan fluorescent protein variants identified by fluorescence lifetime screening. *Nat. Meth.* 7, 137-139
40. Erard, M., Fredj, A., Pasquier, H., Beltolngar, D. B., Bousmah, Y., Derrien, V., Vincent, P., and Merola, F. (2013) Minimum set of mutations needed to optimize cyan fluorescent proteins for live cell imaging. *Mol. BioSys.* 9, 258-267
41. Herbomel, G., Hatte, G., Roul, J., Padilla-Parra, S., Tassan, J. P., and Tramier, M. (2017) Actomyosin-generated tension on cadherin is similar between dividing and non-dividing epithelial cells in early Xenopus laevis embryos. *Sci. Rep.* 7:45058
42. Demeautis, C., Sipieter, F., Roul, J., Chapuis, C., Padilla-Parra, S., Riquet, F. B., and Tramier, M. (2017) Multiplexing PKA and ERK1&2 kinases FRET biosensors in living cells using single excitation wavelength dual colour FLIM. *Sci. Rep.* 7:41026
43. Poea-Guyon, S., Pasquier, H., Merola, F., Morel, N., and Erard, M. (2013) The enhanced cyan fluorescent protein: a sensitive pH sensor for fluorescence lifetime imaging. *Anal. Bioanal. Chem.* 405, 3983-3987
44. Zachariassen, L. G., Katchan, L., Jensen, A. G., Pickering, D. S., Plested, A. J. R., and Kristensen, A. S. (2016) Structural rearrangement of the intracellular domains during AMPA receptor activation. *PNAS* 113, E3950-E3959
45. Valeur, B. (2006) *Molecular Fluorescence, Principles and applications*, 3rd Ed., Wiley-VCH, Weinheim
46. Espagne, A., Erard, M., Madiona, K., Derrien, V., Jonasson, G., Levy, B., Pasquier, H., Melki, R., and Merola, F. (2011) Cyan Fluorescent Protein Carries a Constitutive Mutation That Prevents Its Dimerization. *Biochemistry* 50, 437-439
47. Heikal, A. A., Hess, S. T., Baird, G. S., Tsien, R. Y., and Webb, W. W. (2000) Molecular spectroscopy and dynamics of intrinsically fluorescent proteins: Coral red (dsRed) and yellow (Citrine). *PNAS* 97, 11996-12001
48. Vogel, S. S., van der Meer, B. W., and Blank, P. S. (2014) Estimating the distance separating fluorescent protein FRET pairs. *Methods* 66, 131-138
49. Steinberg, I. Z. (1968) Nonradiative energy transfer in systems in wich rotatory brownian motion is frozen *J. Chem. Phys.* 48, 2411
50. Kenworthy, A. K., and Edidin, M. (1998) Distribution of a Glycosylphosphatidylinositol-anchored Protein at the Apical Surface of MDCK Cells Examined at a Resolution of <100 Å Using Imaging Fluorescence Resonance Energy Transfer. *J. Cell Biol.* 142, 69-84
51. Kenworthy, A. K., Petranova, N., and Edidin, M. (2000) High-resolution FRET microscopy of cholera toxin B-subunit and GPI-anchored proteins in cell plasma membranes. *Mol. Biol. Cell* 11, 1645-1655
52. Zacharias, D. A., Violin, J. D., Newton, A. C., and Tsien, R. Y. (2002) Partitioning of Lipid-Modified Monomeric GFPs into Membrane Microdomains of Live Cells. *Science* 296, 913-916

Accepted manuscript

53. Kofoed, E. M., Guerbadot, M., and Schaufele, F. (2010) Structure, Affinity, and Availability of Estrogen Receptor Complexes in the Cellular Environment. *J. Biol. Chem.* 285, 2428-2437
54. Bohmer, M., Wahl, M., Rahn, H. J., Erdmann, R., and Enderlein, J. (2002) Time-resolved fluorescence correlation spectroscopy. *Chem. Phys. Lett.* 353, 439-445
55. Padilla-Parra, S., Audugé, N., Coppey-Moisan, M., and Tramier, M. (2011) Dual-color fluorescence lifetime correlation spectroscopy to quantify protein–protein interactions in live cell. *Microsc. Res. Techniq.* 74, 788-793
56. Padilla-Parra, S., Auduge, N., Coppey-Moisan, M., and Tramier, M. (2014) Quantitative study of protein-protein interactions in live cell by dual-color fluorescence correlation spectroscopy. *Methods Mol. Biol. (Clifton, N.J.)* 1076, 683-698
57. Konarev, P. V., Volkov, V. V., Sokolova, A. V., Koch, M. H. J., and Svergun, D. I. (2003) PRIMUS: a Windows PC-based system for small-angle scattering data analysis. *J. Appl. Crystallogr.* 36, 1277-1282
58. Petoukhov, M. V., and Svergun, D. I. (2005) Global rigid body modeling of macromolecular complexes against small-angle scattering data. *Biophysical J.* 89, 1237-1250
59. Moore, B. L., Kelley, L. A., Barber, J., Murray, J. W., and MacDonald, J. T. (2013) High-quality protein backbone reconstruction from alpha carbons using gaussian mixture models. *J. Comput. Chem.* 34, 1881-1889
60. Krivov, G. G., Shapovalov, M. V., and Dunbrack, R. L., Jr. (2009) Improved prediction of protein side-chain conformations with SCWRL4. *Proteins* 77, 778-795
61. Tria, G., Mertens, H. D. T., Kachala, M., and Svergun, D. I. (2015) Advanced ensemble modelling of flexible macromolecules using X-ray solution scattering. *IUCrJ* 2, 207-217

Accepted manuscript

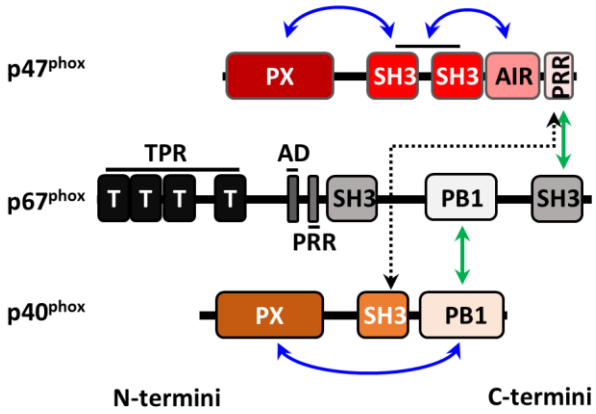


Figure 1. Structural organization of the NADPH oxidase. Domain-structure of the 3 cytosolic subunits of the phagocyte NADPH oxidase in the resting state. The domains and their position in the proteins are drawn approximately to size. Arrows denote known intramolecular interactions (blue) and intermolecular interactions (green). The dashed black line represents the possible interaction between $p40^{phox}$ and $p47^{phox}$.

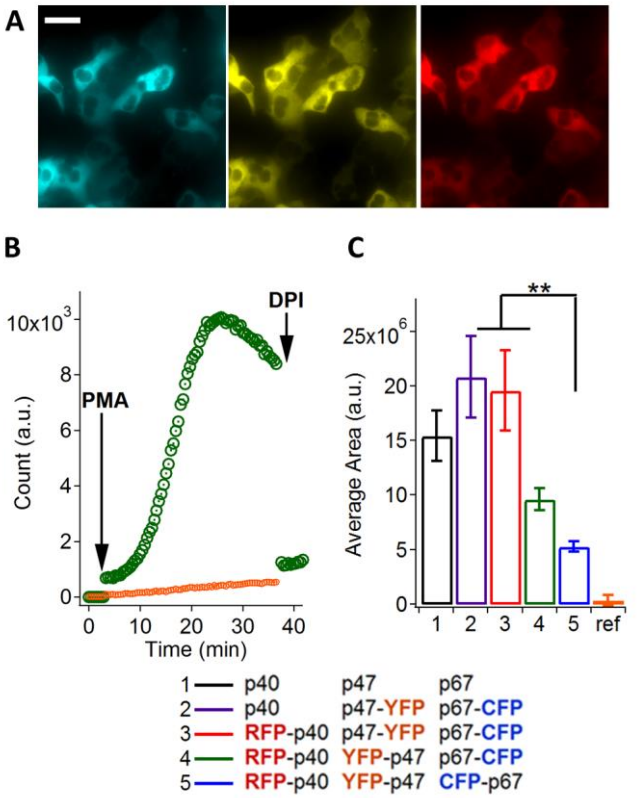


Figure 2. FP-tagged subunits form a functional oxidase. (A) Images of triple-transfected $COS^{Nox2/p22}$ cells expressing $p47^{phox}$-CFP, $p67^{phox}$-YFP, and RFP- $p40^{phox}$ subunits (left to right). Scale bar 20 µm. 5 conditions of $p40^{phox}$, $p47^{phox}$ and $p67^{phox}$ with no tag (x), 2 or 3 tags on either N- or C-terminus were tested. (B) Time course of the luminescence signal (L-012 + HRP) from triple-transfected $COS^{Nox2/p22}$ cells stimulated by PMA and stopped by the oxidase inhibitor DPI at the indicated times (condition 4, green). In orange, the signal obtained with non-transfected cells as reference. (C) Integrated PMA-stimulated luminescence signal over 30 min (n = 3 ; mean ± SEM). **P < 0.01, Tukey's Multiple Comparison Test.

Accepted manuscript

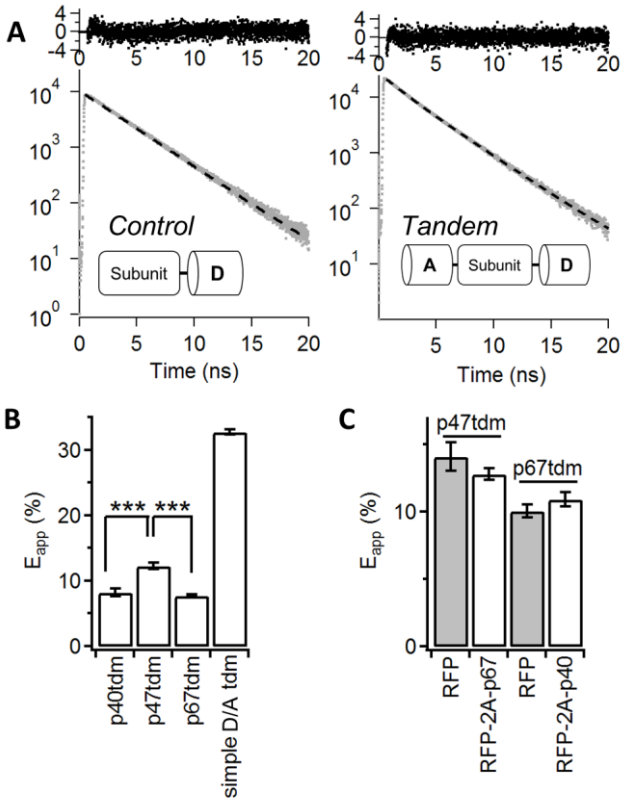


Figure 3. Efficient FRET between N- and C-terminal tags on all subunits (tandem). (A) Representative example of fluorescence decays of the tandems and their fits (dashed line). The upper panels show the residual difference plot. For $p40^{phox}$, a YFP/RFP FRET pair was used, while $p47^{phox}$, $p67^{phox}$, and the simple D/A tandem were labelled with a CFP/YFP FRET pair. The control shown on the left is $p40^{phox}$-YFP (τ_{donor} = 3.18 ns, χ^2 = 1.12), while the tandem shown on the right is RFP-$p40^{phox}$-YFP, (τ_{long} = 3.17 ns, τ_{short} = 1.56 ns, accounting for 77% and 23 % of the decay amplitude respectively, χ^2 = 1.09). (B) Apparent FRET efficiencies for $p40^{phox}$, $p47^{phox}$ and $p67^{phox}$ tandems and the positive control (simple D/A tandem). (C) Effect of $p67^{phox}$ co-expression on the $p47^{phox}$ tandem and of $p40^{phox}$ on the $p67^{phox}$ tandem. A co-transfection of the tandem with RFP alone was used as control (n = 10-30 cells ; mean ± SEM, raw data Fig. S2). ***P < 0.001, Tukey's Multiple Comparison Test.

Accepted manuscript

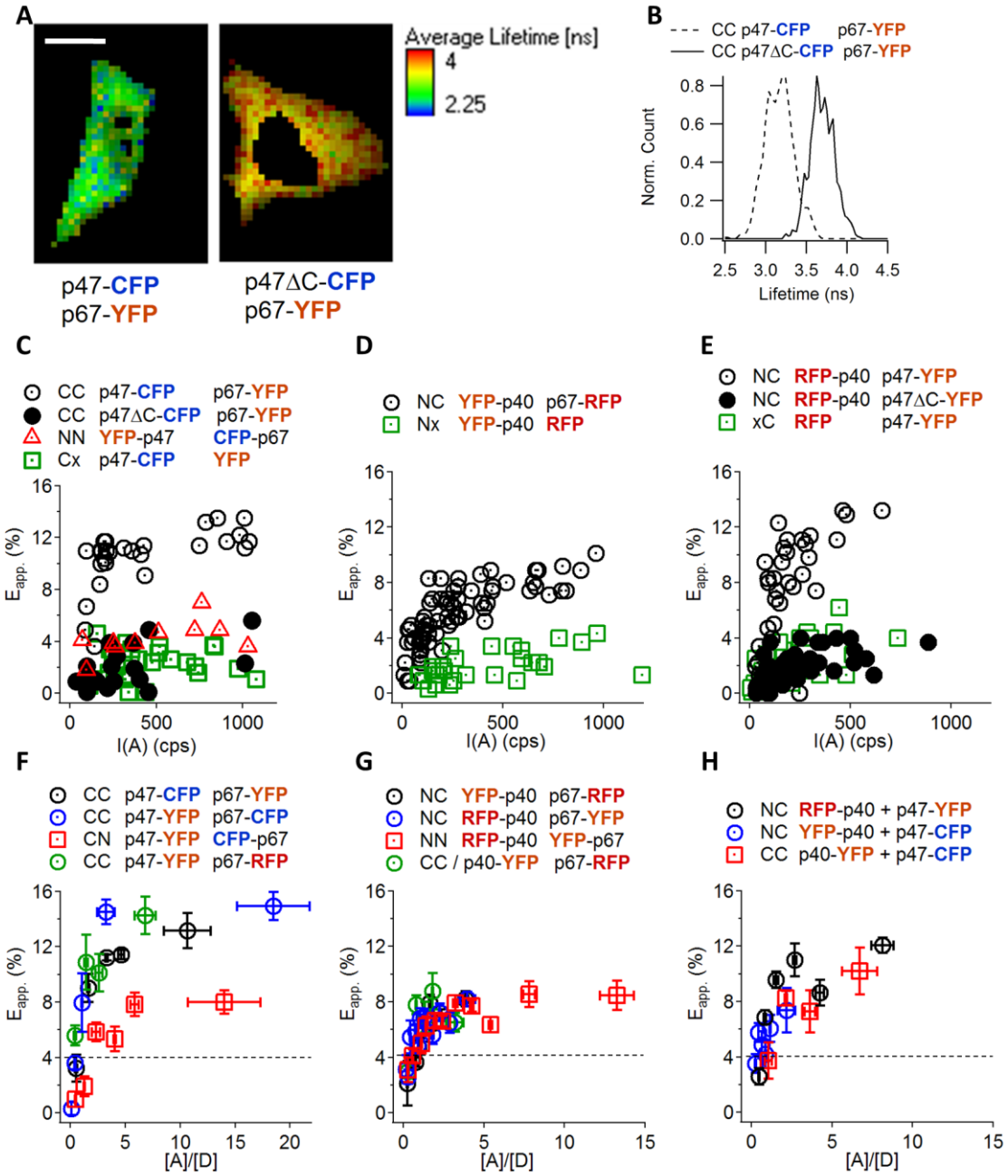


Figure 4. FRET reveals heterodimer formation between all subunits. (A) Representative fluorescence lifetime images of COS7 cells expressing p47-CFP (left) or p47ΔC-CFP with p67-YFP (right), scale bar 10 µm. (B) Corresponding histograms of fluorescence lifetimes over the image pixels. The lifetime of p47-CFP (donor alone) is 3.95 ± 0.05 ns. (*C-E*) FRET-efficiencies plotted against acceptor intensity, each symbol represents the value for one cell. (*F-H*) FRET-efficiencies plotted against acceptor/donor ratio, each symbol represents the mean ± SEM of 3 to 6 cells. The dashed lines indicate the upper limit of the negative controls shown as green squares in C-E. Left (C, F): interaction of $p47^{phox}$ and $p67^{phox}$; center (D, G): interaction of $p40^{phox}$ and $p67^{phox}$; right (E, H): interaction of $p40^{phox}$ and $p47^{phox}$.

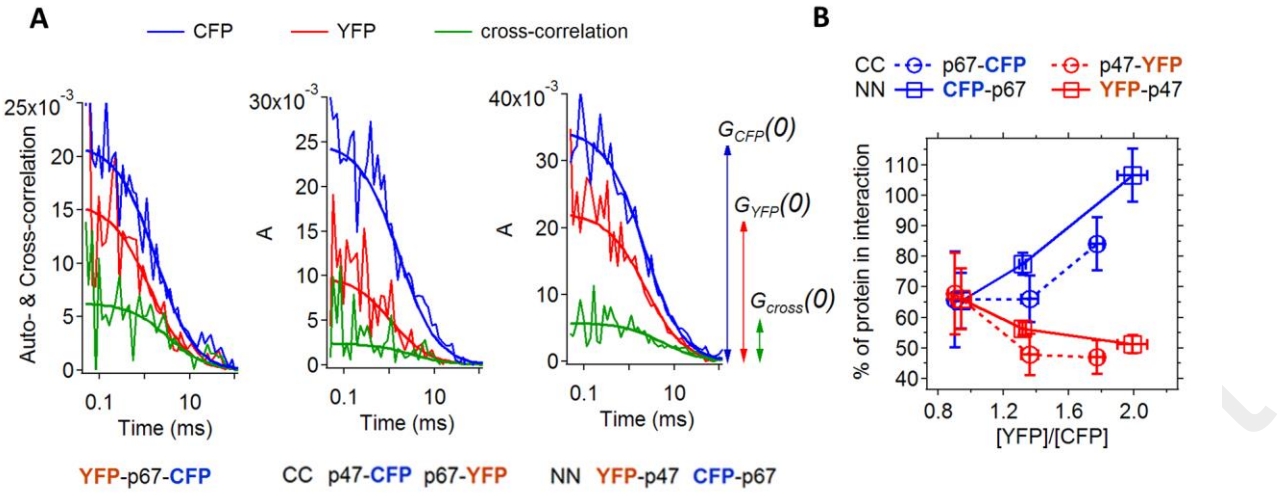


Figure 5. FCCS demonstrates that all p67^{phox} is in complex with p47^{phox}. (A) Example of auto-correlation and cross-correlation functions and their fits from individual cells. FCCS-data from COS7 cells transfected with the p67^{phox} tandem (left) or p47^{phox} together with p67^{phox} (middle, right). We use the p67^{phox} tandem as a positive control for co-diffusion. (B) Fraction of protein in interaction, as a function of YFP:CFP ratio, as obtained from the correlation functions. At twofold excess of p47-YFP, all p67-CFP is in complex and 50% of p47-YFP is in complex. Each symbol represents the mean ± SEM of 5 to 10 cells from 3 independent experiments. We chose cells expressing YFP tagged p47^{phox} in varying quantities while keeping the CFP tagged p67^{phox} concentration at a nearly constant low level. This simulates the situation in neutrophils, where the expression of p47^{phox} is higher than p67^{phox} (32).

Accepted manuscript

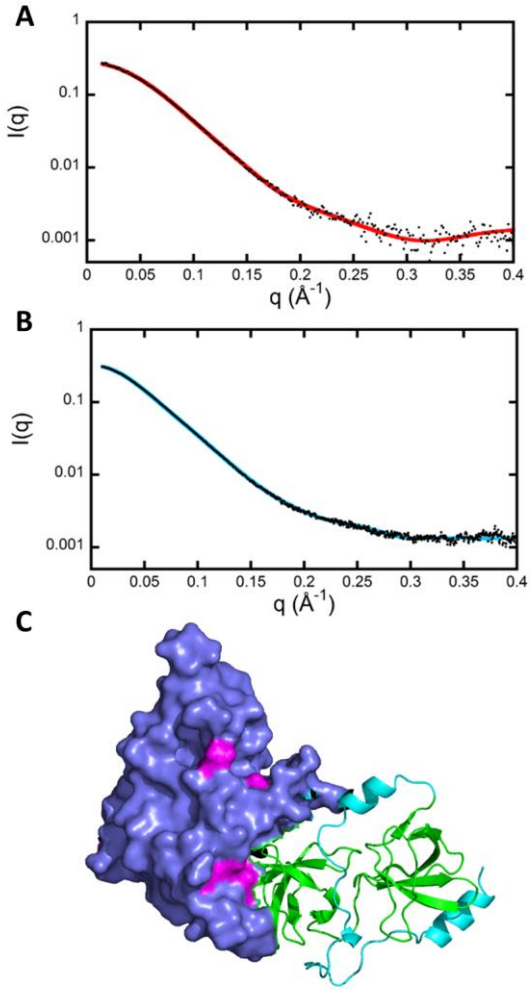


Figure 6. Modeling of p47^{phox}ΔCter from SAXS data. (A) Experimental SAXS curve measured on p47^{phox}ΔCter (black dots), compared to the calculated curve (red line) obtained from the selected model shown in (C) using the program CRYSOL (χ^2=0.97). (B) Experimental SAXS curve measured on full-length p47^{phox} (black dots) compared to the theoretical curve (blue line) calculated from the model of p47^{phox} shown in Fig. 7 (χ^2=1.25). (C) Selected SAXS model of p47^{phox}ΔCter that fulfills all the criteria discussed in the text and in Fig. S6. PX domain in violet, SH3 domains in green, AIR domain in cyan. Residues of the PX domain responsible for interaction with the membrane in the activated form are shown in pink.

Accepted manuscript

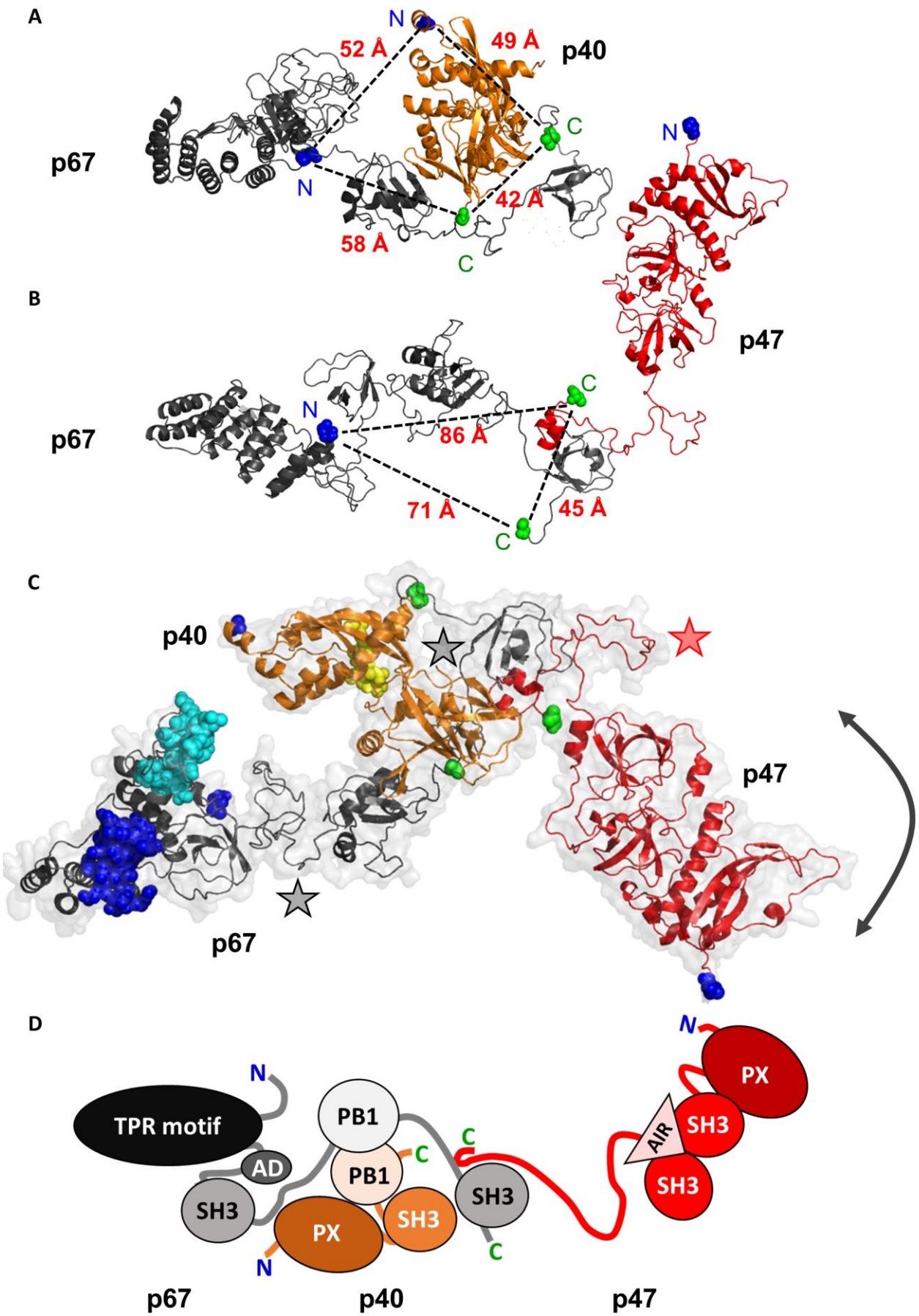


Figure 7. Proposed model of the complete cytosolic complex of phagocyte NADPH oxidase in the inactive state. Ribbon representation of $p40^{phox}$ (orange), $p47^{phox}$ (red), $p67^{phox}$ (grey). The N-termini

are labelled in blue and the C-termini are labelled in green. Pairwise interactions are shown (A) between $p40^{phox}$ and $p67^{phox}$ and (B) between $p47^{phox}$ and $p67^{phox}$, while the whole 3D-model of the hetero-trimer is shown in (C). Distances between termini, as predicted from the proposed model, are only given for model evaluation (see text). The arrow symbolizes the angular flexibility of the globular N-terminal domain of $p47^{phox}$. The stars indicate the flexible regions in $p67^{phox}$ (black stars) and in $p47^{phox}$ C-terminus (red star). In $p67^{phox}$, blue and cyan spheres represent the Rac-binding β-hairpin insertion and the activation domains respectively. The residues of the PX domains interacting with lipids in $p40^{phox}$ are the yellow spheres. (D) Schematic representation of the complex showing the different functional domains.

Accepted manuscript

Quantitative live-cell imaging and 3D modeling reveal critical functional features in the cytosolic complex of phagocyte NADPH oxidase

Cornelia S Ziegler, Leila Bouchab, Marc Tramier, Dominique Durand, Franck Fieschi, Sophie Dupré-Crochet, Fabienne Mérola, Oliver Nüße and Marie Erard

J. Biol. Chem. published online January 10, 2019

Access the most updated version of this article at doi: 10.1074/jbc.RA118.006864

Alerts:
- When this article is cited
- When a correction for this article is posted

Click here to choose from all of JBC's e-mail alerts

Accepted manuscript